



Highly active subnanometer Rh clusters derived from Rh-doped SrTiO₃ for CO₂ reduction



Binhang Yan^{a,b,1}, Qiyuan Wu^{c,1}, Jiajie Cen^c, Janis Timoshenko^c, Anatoly I. Frenkel^{b,c}, Dong Su^d, Xianyin Chen^e, John B. Parise^e, Eric Stach^d, Alexander Orlov^{c,*}, Jingguang G. Chen^{b,f,*}

^a Department of Chemical Engineering, Tsinghua University, Beijing 100084, China

^b Chemistry Department, Brookhaven National Laboratory, Upton, NY 11973, USA

^c Department of Materials Science and Chemical Engineering, Stony Brook University, Stony Brook, NY 11794, USA

^d Center for Functional Nanomaterials, Brookhaven National Laboratory, Upton, NY 11973, USA

^e Chemistry Department, Stony Brook University, Stony Brook, NY 11794, USA

^f Department of Chemical Engineering, Columbia University, New York, NY 10027, USA

ARTICLE INFO

Keywords:

CO₂ reduction

Subnanometer

Perovskite

Doping-segregation

Selectivity

ABSTRACT

Sub-nanometer Rh clusters derived from Rh-doped SrTiO₃, demonstrated by *in-situ* X-ray Diffraction (XRD) and X-ray Absorption Fine Structure (XAFS) measurements, are applied as highly active catalysts for CO₂ reduction. Compared to the supported Rh/SrTiO₃, the catalyst synthesized by a doping-segregation method exhibits a higher space-time yield (STY) to CO with a selectivity of 95% for CO₂ reduction by hydrogen; it also shows a higher activity with a larger turnover frequency (TOF) for CO₂ reduction by ethane. According to the *in-situ* diffuse reflectance infrared Fourier transformed spectroscopy (DRIFTS) experiments, the higher CO selectivity for CO₂ hydrogenation is attributed to the lower CO binding strength resulted by the strong interactions (e.g., charge transfer) between Rh atoms and the oxide support with surface defects. The superior activity is suggested to be originated from the cooperative effect between the highly dispersed sub-nanometer Rh clusters for efficient dissociation of H₂/C₂H₆ and the reconstructed SrTiO₃ with oxygen vacancies for preferential adsorption/activation of CO₂. The doping-segregation method provides a unique opportunity to tune the size of active metal clusters and the physicochemical properties of the oxide support, offering the potential for applications in a variety of chemical reactions.

1. Introduction

The rising level of CO₂ in the atmosphere is forecasted to have disastrous effects on global climate change and ocean acidification [1,2]. To stabilize atmospheric CO₂ concentration, it is necessary to significantly reduce fossil-fuel CO₂ emissions and efficiently remove CO₂ from the atmosphere, such as the catalytic reduction of CO₂ to valuable chemicals [2,3]. One proven route is converting CO₂ to CO (or syngas), which can be used as feedstock to produce value-added chemicals and synthetic fuels in the Fischer-Tropsch (FT) process. It is well known that CO₂ can be reduced to CO using hydrogen via the reverse water gas shift (RWGS) reaction [4,5] or be converted to syngas by light alkanes from shale gas (e.g., ethane) via the dry reforming reaction [6,7].

Supported precious metal catalysts (e.g., Rh, Pt, Pd) have been

extensively explored for CO₂ reduction either by hydrogen [8–11] or light alkanes [12–14]. For catalytic conversion of CO₂ over supported precious metal catalysts, it is generally accepted that CO₂ is primarily adsorbed and activated on the oxide support or metal-oxide interface [5,15], while the precious metal sites facilitate the dissociation of hydrogen or alkane molecules. Therefore, efficient reduction of CO₂ requires a dual functional catalyst with high activity for both C–O bond scission and hydrogen/alkane dissociation. It has been previously shown that compared to irreducible oxides (e.g., γ -Al₂O₃), reducible oxides (e.g., CeO₂) supported precious metal catalysts were more active for CO₂ conversion either by hydrogen [8] or ethane [7]. This can be explained by reduced oxides with surface defects or oxygen vacancies having a strong tendency to react with CO₂, enabling direct C–O bond scission pathway. Meanwhile, the size of metal particles is also a critical factor in determining the catalytic performance as underscored by the

* Corresponding author at: Department of Chemical Engineering, Columbia University, New York, NY, 10027, USA.

** Corresponding author at: Department of Materials Science and Chemical Engineering, Stony Brook University Stony Brook, NY 11794, USA.

E-mail addresses: alexander.orlov@stonybrook.edu (A. Orlov), jgchen@columbia.edu (J.G. Chen).

¹ These authors contributed to the work equally.

activity for hydrogen/alkane dissociation generally increasing with decreasing size of the metal particles [16]. Furthermore, as the particle size is decreased from nanometer to subnanometer scale (less than 1 nm, which is defined as the subnanometer cluster in this work), the catalytic activity and/or selectivity may change significantly due to the low-coordination environment, quantum size effect, and improved metal-support interactions [16,17]. Supported subnanometer metal catalysts have exhibited better catalytic activity and/or modified selectivity as compared to that for nanometer-sized metal catalysts [9,18–20]. For a specific case of CO₂ hydrogenation reaction, experimental results indicate that the atomically dispersed Rh sites deposited on TiO₂ support exhibited significantly different product selectivity as compared to that of the larger TiO₂ supported Rh nanoparticles [9].

Supported metal nanoparticles can be synthesized by a doping-segregation method using perovskite oxides (ABO₃) [21–24]. The active metal atoms are firstly doped into the lattice of perovskite oxides to substitute the B-site atoms, where the active metal cations are atomically dispersed. These metal cations can be then segregated to form metal clusters during the subsequent reduction process. Here we present a subnanometer Rh catalyst derived from Rh-doped SrTiO₃ with a superior catalytic performance for CO₂ reduction by H₂ and C₂H₆. To benchmark its catalytic performance, the Rh/SrTiO₃ catalyst synthesized by the traditional method of wetness impregnation was also studied. The successful doping of Rh atom into the SrTiO₃ lattice and the formation of subnanometer Rh clusters were demonstrated by *ex-situ* X-ray Diffraction (XRD), Raman, Ultraviolet-Visible (UV-vis) spectroscopy, Scanning Transmission Electron Microscopy (STEM), and *in-situ* XRD and X-ray Absorption Fine Structure (XAFS) measurements. The reduced Rh-doped SrTiO₃ catalyst exhibited an enhanced space-time yield and selectivity to CO for CO₂ hydrogenation at 573 K and a higher activity for dry reforming of ethane (DRE) at 823 K, as compared to those of the supported Rh/SrTiO₃ catalyst. Further experimental results suggest that the superior catalytic activity and selectivity facilitated by the highly dispersed subnanometer Rh clusters enhancing efficient dissociation of H₂/C₂H₆, the restructured SrTiO₃ with oxygen vacancies promoting preferential adsorption/activation of CO₂, and catalyst-support effects displaying delicate interplay between Rh atoms strongly interacting (e.g., charge transfer) with support containing surface defects, leading to weakening of the Rh–CO bond.

2. Experimental methods

2.1. Catalyst synthesis

Rh-doped SrTiO₃ powders were synthesized by a hydrothermal (HT) method. Strontium hydroxide octahydrate (Sigma-Aldrich, 95%), titanium dioxide (Sigma-Aldrich, nanopowder, 21 nm, ≥99.5%), and rhodium (III) nitrate hydrate (Sigma-Aldrich, ~36% rhodium basis) were used as the starting materials with a molar ratio of Sr : Ti : Rh = 1.10 : 0.98 : 0.02. In a typical synthesis to yield 1.468 g (4 mmol) Rh-doped SrTiO₃ (2 mol% Rh doped), TiO₂ (0.313 g, 3.92 mmol) was suspended in 15 mL of DI water. While the suspension was continuously stirred, Sr(OH)₂·8H₂O (1.169 g, 4.4 mmol) was added. Then Rh(NO₃)₃ (23.12 mg, 0.08 mmol) dissolved in 2 mL of DI water was subsequently introduced. The final suspension was sonicated for 10 min and then poured in a PTFE-lined stainless steel acid digestion vessel (model PA4749, volume 23 mL, Parr Instrument Company). The vessel was heated at 473 K at about 10 K/min and then kept at 473 K for a time ranging from 24 h to 48 h. After cooling, the vessel was opened and the reaction product was centrifuged and washed several times with DI water. The product was then dried at 343 K overnight. The sample was denoted as HT-2 and the reduced sample was denoted as HT-2-R.

To synthesize a benchmark catalyst, a supported Rh/SrTiO₃ catalyst was synthesized by wetness impregnation over as-is commercial support (SrTiO₃, Sigma-Aldrich, nanopowder) with an aqueous solution of Rh(NO₃)₃. After impregnation, the catalyst was dried at 363 K for 12 h,

then ramped to 723 K with a rate of 0.8 K/min and calcined for 4 h in air. The metal loading amount and atomic ratio for these two catalysts were kept the same, as listed in Table S1.

2.2. Ex-situ characterization

Ex-situ XRD was conducted using Cu K α radiation ($\lambda = 1.54056 \text{ \AA}$, Rigaku Ultima III). Ultraviolet-visible light (UV-vis) diffuse reflectance spectroscopy (Thermo Evolution 300) was used to characterize the electronic structure of synthesized samples. Additional analysis was carried out by Raman spectroscopy (WiTec Probe Microscope) using 632.5 nm radiation. Transmission electron microscopy (TEM) was conducted using JEOL 2100 F TEM operated at 200 kV and scanning transmission electron microscopy (STEM) was carried out using a Hitachi HD2700C dedicated STEM operating at 200 kV with a probe aberration-corrector.

Pulse CO chemisorption experiments were performed in an Altamira AMI-300 ip catalyst characterization system. Approximately 100 mg of fresh catalyst loaded in a U-shaped quartz tube was firstly dried in a helium flow (30 mL/min) at 393 K for 30 min, and then reduced at 573 K for 60 min using a mixture of 5% H₂ in Ar (30 mL/min). The reduced catalyst was purged with He (50 mL/min) for degassing and then cooled down to 313 K. Pulses of 10% CO in He (590 μL loop) were injected into the He stream until the CO peak became constant. The amount of CO flowing out of the reactor was monitored by a thermal conductivity detector (TCD). The CO uptake values for both catalysts are listed in Table S1.

2.3. In-situ characterization

2.3.1. In-situ XRD analysis

In-situ XRD analysis was carried out using of a Rigaku Ultima IV diffractometer (Cu K α radiation, $\lambda = 1.54056 \text{ \AA}$) equipped with a D/TeX high-speed linear position sensitive detector, a Rigaku XRD-DSC stage, a ULVAC vacuum pump, and a vacuum manifold. It is organized such that the desired gas flows from the selection manifold through a flow meter where mass flow controllers balance the mixing of flow gases [25]. During the XRD collection process, the HT-2 sample was treated *in-situ* on the XRD-DSC stage by heating under a mixing gas flow (4% H₂/He) at a rate of 1 K/min to 723 K. The powder XRD patterns were collected by an *in-situ* XRD system at a rate of 0.01 °/min with a 0.001-degree step size over the 20 range from 31 to 34 degrees.

2.3.2. In-situ X-ray absorption fine structure (XAFS) measurements

In-situ Rh K-edge (23,230 eV) XAFS spectra for Rh-doped SrTiO₃ samples were acquired at SSRL beamline BL2-2. For this experiment, the HT-2 sample in powder form was mixed with boron nitride and pressed into a pellet. The pellet was then mounted in a Nashner-Adler cell [26] for heating and *in-situ* XAFS measurements. Three sets of XAFS spectra were acquired: for as-synthesized sample at room temperature, heated for 30 min at 573 K, and cooled back to room temperature. All measurements and sample heating were performed in 5% H₂ (diluted in He) flow at the rate of 40 mL/min. A double crystal Si (220) monochromator was used for energy selection. The X-ray beam size was 4 mm (horizontally) by 0.25 mm (vertically). Measurements were performed in the transmission mode. XAFS spectra of bulk Rh foil, located between two ionization chambers downstream from the sample, were measured in the same experiment and used as a reference for absolute energy calibration and alignment purposes. The experimental Rh K-edge XAFS spectra were extracted, aligned, and processed by conventional procedures using Athena software. Data analysis was done by linear combination fitting of the X-ray absorption near edge structure (XANES) data, using Athena, and non-linear least square fitting of extended X-ray absorption fine structure (EXAFS) data, using Artemis software [27].

2.3.3. In-situ DRIFTS studies

In-situ DRIFTS experiments were performed using FTIR spectrometer (Thermo, Nicolet 6700). Approximately 20 mg of fine catalyst powder (< 80 mesh) was carefully packed into the sample holder and the surface was smoothly flattened to enhance IR reflection. With the cell securely located in the FTIR instrument, the catalyst was first reduced at 573 K for 40 min in a 5% H₂/He mixture (20 mL/min). A background spectrum (512 scans) with a resolution of 4 cm⁻¹ was then obtained in the mid-infrared range (650–4000 cm⁻¹) under the reduction conditions for each sample. The in-situ DRIFT spectra for CO₂ hydrogenation at 573 K were recorded by collecting 128 scans at 4 cm⁻¹ resolution, according to the following procedure: (1) in-situ reaction (5% H₂, 5% CO₂, 20 mL/min) for 40 min; (2) H₂ purge/treatment (5% H₂, 20 mL/min) for 40 min. The in-situ DRIFT spectra shown in this work were expressed in units of Kubelka-Monk.

2.4. Flow reactor evaluation

2.4.1. Steady state studies

Flow reactor studies were performed in a quartz tube reactor with an inner diameter of 4 mm under atmospheric pressure. For steady state experiments, ~20 mg of sieved catalyst (60–80 mesh) mixed with ~180 mg inert material (acid-purified quartz that was pre-calcined at 1173 K for 2 h, 60–80 mesh) was loaded into a reactor tube and held in place by quartz wool. The concentrations of gas products were analyzed on-line by a gas chromatography (Agilent 7890B) equipped with a flame ionization detector (FID) and a TCD.

For CO₂ + H₂ experiments, CO₂ and H₂, diluted with 36 mL/min Ar, were set at 1:1 ratio (2 mL/min CO₂ with 2 mL/min H₂). The catalysts were first reduced under a 5% H₂/Ar mixture at 573 K for 60 min prior to reaction. Then the inlet flow was switched to reactants and held at 573 K for 13 h. In order to compare the selectivity of these two catalysts at a similar CO₂ conversion, the experiment with higher loading of Rh/SrTiO₃ (100 mg) catalyst under the same reaction conditions was also performed.

For CO₂ + C₂H₆ experiments, Ar was introduced into the reactor as a diluent at a flow rate of 10 mL/min, CO₂ and C₂H₆ were set at 2:1 ratio (20 mL/min CO₂ with 10 mL/min C₂H₆). Both catalysts were reduced under a 5% H₂/Ar mixture (2 mL/min H₂ with 38 mL Ar) at 573 K for 60 min prior to reaction. Then the temperature was increased at a rate of 10 K/min and held at 823 K in the presence of reactants for 13 h. After the steady-state measurement, the reaction temperature was changed from 823 K to 773 K with 10 K increments, in order to study the effect of temperature on the reaction rate of CO₂ and ethane. More details are provided in the Supplementary Material Section S2.

2.4.2. Pulse reactor studies

The isothermal pulse experiments were performed at 823 K using a quartz tube reactor. Approximate 20 mg sample was used for each experiment. Prior to the pulse reaction, the catalysts were first reduced at 823 K in a 20 mL/min 5% H₂/Ar flow for 30 min. After being purged with an Ar flow for 10 min, 12 pulses of 10% CO₂/N₂ were injected into the reactor via a 1 mL gas loop. The products flowing out of the reactor were analyzed by a gas chromatography (Agilent 7890B) equipped with FID and TCD.

3. Results and discussion

3.1. Formations of subnanometer Rh clusters from Rh-doped SrTiO₃

The crystal phase of the HT-2 sample was first examined by *ex-situ* XRD. The XRD pattern of the HT-2 sample is shown in Fig. 1a along with the standard diffraction pattern of SrTiO₃ (JCPDS# 35-0734). The synthesized sample exhibited the diffraction pattern typical for those of cubic perovskite structure and all the diffraction peaks could be indexed to the XRD pattern of the standard perovskite SrTiO₃ phase as shown in

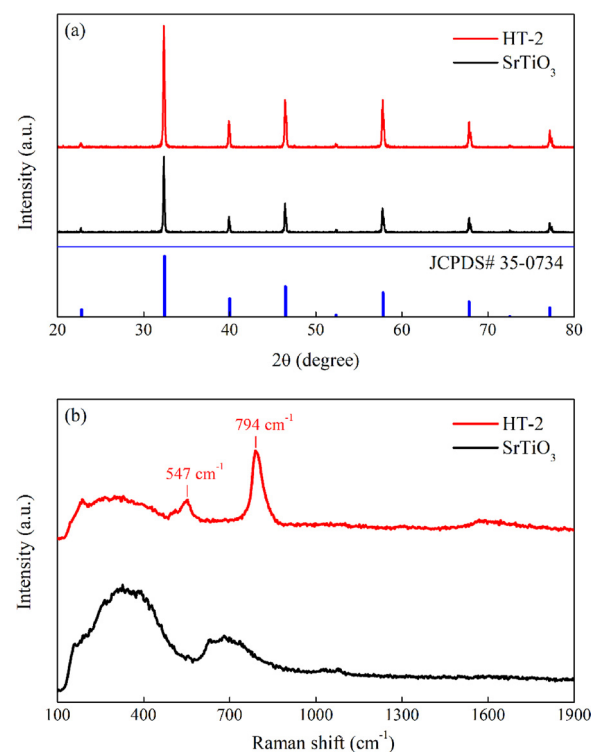


Fig. 1. (a) XRD patterns and (b) Raman spectra of the synthesized pristine SrTiO₃ and HT-2 samples.

Fig. 1a. Following the confirmation of the cubic perovskite phase of the HT-2 sample, the successful doping of Rh atoms was then confirmed by *ex-situ* Raman spectroscopy. Fig. 1b shows the Raman spectrum of the HT-2 sample along with a spectrum of an undoped SrTiO₃ sample for comparison. A comparison of the spectrum of the doped sample to that of a pristine SrTiO₃ sample highlights new first-order Raman scattering peaks centered at 547 and 794 cm⁻¹ in the spectrum of the HT-2 sample, which indicates a successful substitutional doping of Rh atoms into the SrTiO₃ lattice by replacing Ti atoms [28,29]. The successful synthesis of Rh-doped SrTiO₃ was also confirmed by *ex-situ* UV-vis spectroscopy, as shown in Fig. S1 in Supplementary Material.

After confirming the successful synthesis of Rh-doped SrTiO₃, the reductive segregation of Rh atoms from the perovskite lattice to form Rh clusters was examined by using various *in-situ* characterization techniques. The evolution of the SrTiO₃ lattice during the reductive segregation was first studied using *in-situ* XRD. Fig. 2 shows the lattice parameter of the HT-2 sample as a function of temperature during reductive heating under a 4% H₂ flow. The lattice parameter was

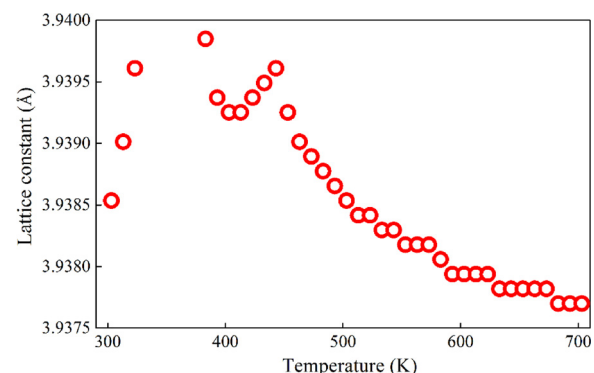


Fig. 2. Evolution of the lattice parameter of cubic perovskite structure for the HT-2 sample during reductive heating. The lattice constant was calculated from the position of (110) plane reflection.

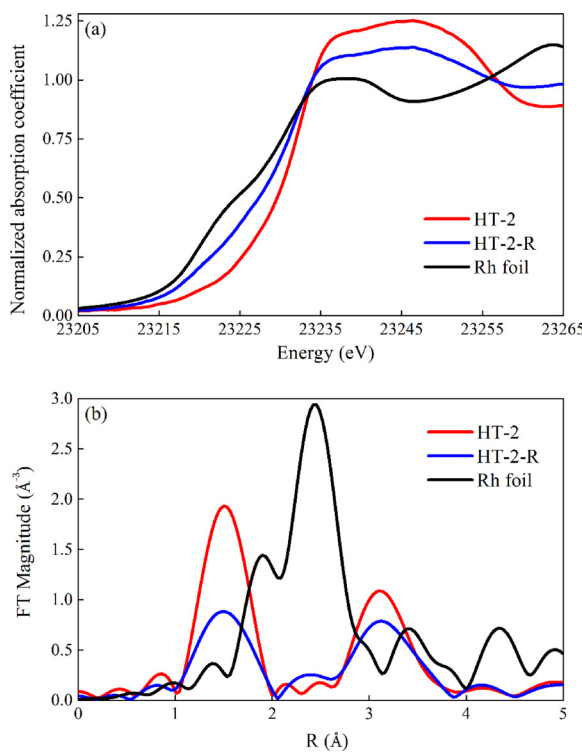


Fig. 3. *In-situ* XAFS data of Rh foil, the HT-2 and HT-2-R samples: (a) XANES region, and (b) Fourier transform magnitudes of the k^2 -weighted EXAFS data.

calculated from the position of the (110) plane reflection. During the ramping of temperature, the lattice of HT-2 first expanded, then underwent a quick shrinking process, which plateaued at 573 K, as shown in Fig. 2. The expansion of the lattice was caused by the thermal effect, while the shrinkage of lattice indicated the expulsion of Rh dopant atoms from the lattice of HT-2.

In-situ XAFS measurement was then conducted to understand from the local structure perspective the segregation of Rh dopant atoms during reductive heating. Fig. S2 presents the Rh K-edge XAFS spectra of the HT-2 sample before and after *in-situ* reduction along with two standard samples. XAFS spectra demonstrate that the state of Rh in perovskite before reduction is non-metallic. Furthermore, the local environment of Rh atoms is different from that in Rh_2O_3 . As shown in Fig. S2, the peak at 3.2 Å is likely contributed from the Rh-O-Ti linkage as expected, given that Rh dopant atoms substitute for Ti atoms in the $SrTiO_3$ lattice, as ascertained by Raman spectroscopy (vide supra). The XANES spectra of the HT-2 sample before and after *in-situ* reduction, together with that of Rh foil, are plotted in Fig. 3a. As seen in Fig. 3a, the presence of multiple isosbestic points indicates that the reduced sample is likely a mixture of the Rh-doped $SrTiO_3$ and metallic Rh phases. The volume mixing fractions of each phase were thus obtained by using a linear combination fitting (LCF) analysis, indicating that about 45% of Rh atoms were in the metallic Rh phase. However, the use of the bulk Rh foil XANES spectrum as one of the two standards in Fig. 3a for LCF analysis leads to the underestimation of the reduced phase, hence, the results of the LCF analysis are presented for qualitative purpose only. The local structural parameters were estimated by the analysis of the EXAFS region in the absorption spectra. The details of the modeling are given in the Supplementary Material as well as the plots of the data in both k -space and R-space along with the theoretical fits (Fig. S3). Before the *in-situ* reduction, the EXAFS spectrum was dominated by the substitutional state of Rh in the $SrTiO_3$ lattice, as shown in Fig. 3b. Theoretical fitting results (Table 1 and Fig. S3) indicate that the Rh-O coordination number (CN) before reduction was somewhat less than the expected value of 6 (in an ideal perovskite

Table 1
EXAFS fitting results of the HT-2 and HT-2-R samples.

Sample	Shell	CN	Bond length (Å)	σ^2 (Å ²)	ΔE_0 (eV)
HT-2	Rh-O	4.7 ± 1.2	2.03 ± 0.02	0.000 ± 0.003	-4.0 ± 3.4
HT-2-R	Rh-O	2.5 ± 0.5	2.05 ± 0.01	0.001 ± 0.002	-4.6 ± 1.5

structure), namely: 4.7 ± 1.2 , which is reasonable because the substitutional doping of Rh atoms replacing Ti atoms in the $SrTiO_3$ lattice would lead to the possible formation of oxygen vacancy [29]. After *in-situ* reduction, the fitting results indicate that the Rh-O CN decreases to 2.5 ± 0.5 , suggesting the removal of Rh dopant atoms from the $SrTiO_3$ sites, which is consistent with the *in-situ* XRD results. Moreover, the Rh-O CN of the reduced sample is about 50% of that of the fresh sample, revealing that approximately half of the Rh atoms still remain in the $SrTiO_3$ lattice, which also agrees qualitatively with the LCF analysis result based on XANES region. The contribution of Rh-Rh paths in the theoretical fitting was found to be negligible, suggesting that the formed Rh clusters might be extremely small.

In order to examine the hypothesis based on the EXAFS analysis, high-resolution STEM imaging of the HT-2-R sample was conducted. Fig. 4a and b show the dark-field STEM images of the HT-2-R sample with different magnifications. The formed Rh clusters after reduction are extremely small and with sizes on the subnanometer scale, as suggested by the EXAFS analysis. Scanning electron microscopy (SEM) signal during STEM imaging was collected in order to confirm that the formed Rh clusters were on the surface of $SrTiO_3$, as shown in Fig. 4c. The average diameter of formed Rh clusters on HT-2-R is 0.89 ± 0.14 nm. As a comparison, high-resolution TEM imaging was also conducted on the reduced Rh/ $SrTiO_3$ sample to determine the particle size. The TEM images are shown in Fig. 4e–g, and the average diameter of Rh nanoparticles on Rh/ $SrTiO_3$ is 4.14 ± 0.93 nm.

3.2. Catalytic activity of HT-2-R for CO_2 hydrogenation

The flow reactor experiments of CO_2 hydrogenation reaction over HT-2-R and Rh/ $SrTiO_3$ were carried out under atmospheric pressure at 573 K. The conversions of CO_2 and H_2 , and yields of CO and CH_4 as a function of time on stream for both samples are shown in Fig. S4. The TOFs of CO_2 and H_2 , STYs of CO and CH_4 as a function of time on stream for both samples are shown in Fig. 5. The steady-state conversion, yield, selectivity, turnover frequency (TOF) and space-time yield (STY) are listed in Table 2. Due to the formation of highly dispersed subnanometer Rh clusters (0.89 ± 0.14 nm), HT-2-R shows not only a much higher activity for CO_2 hydrogenation but also a higher selectivity to CO production than those for Rh/ $SrTiO_3$ under same conditions in terms of the steady-state conversion, yield, STY and TOF. In order to compare the selectivity of these two catalyst at a similar conversion, a control experiment with higher loading (100 mg) of Rh/ $SrTiO_3$ sample under the same reaction conditions was performed. As summarized in Table 2, the CO selectivity on HT-2-R (95.4%) was much higher than that on Rh/ $SrTiO_3$ (56.1%), suggesting that CO formation is more favorable on HT-2-R while CH_4 formation was more favorable on Rh/ $SrTiO_3$. Overall, the flow reactor results indicate that HT-2-R is a promising catalyst with superior activity for highly selective reduction of CO_2 to CO .

To study the effects of Rh particle size and support defect (e.g., oxygen vacancy) on product selectivity, *in-situ* DRIFTS experiments for CO_2 reduction by hydrogen over HT-2-R and Rh/ $SrTiO_3$ were performed. Fig. 6 shows the transient evolution of the principal surface species on HT-2-R and Rh/ $SrTiO_3$ catalysts during CO_2 hydrogenation at 573 K after 30 min H_2 reduction, and Fig. 7 shows a similar data for HT-2-R and Rh/ $SrTiO_3$ catalysts after switching the $CO_2 + H_2$ reactants to a 5% H_2 flow at 573 K. The intensities of the main peaks in Figs. 6 and 7 as a function of time are shown in Figs. S5 and S6, respectively. As

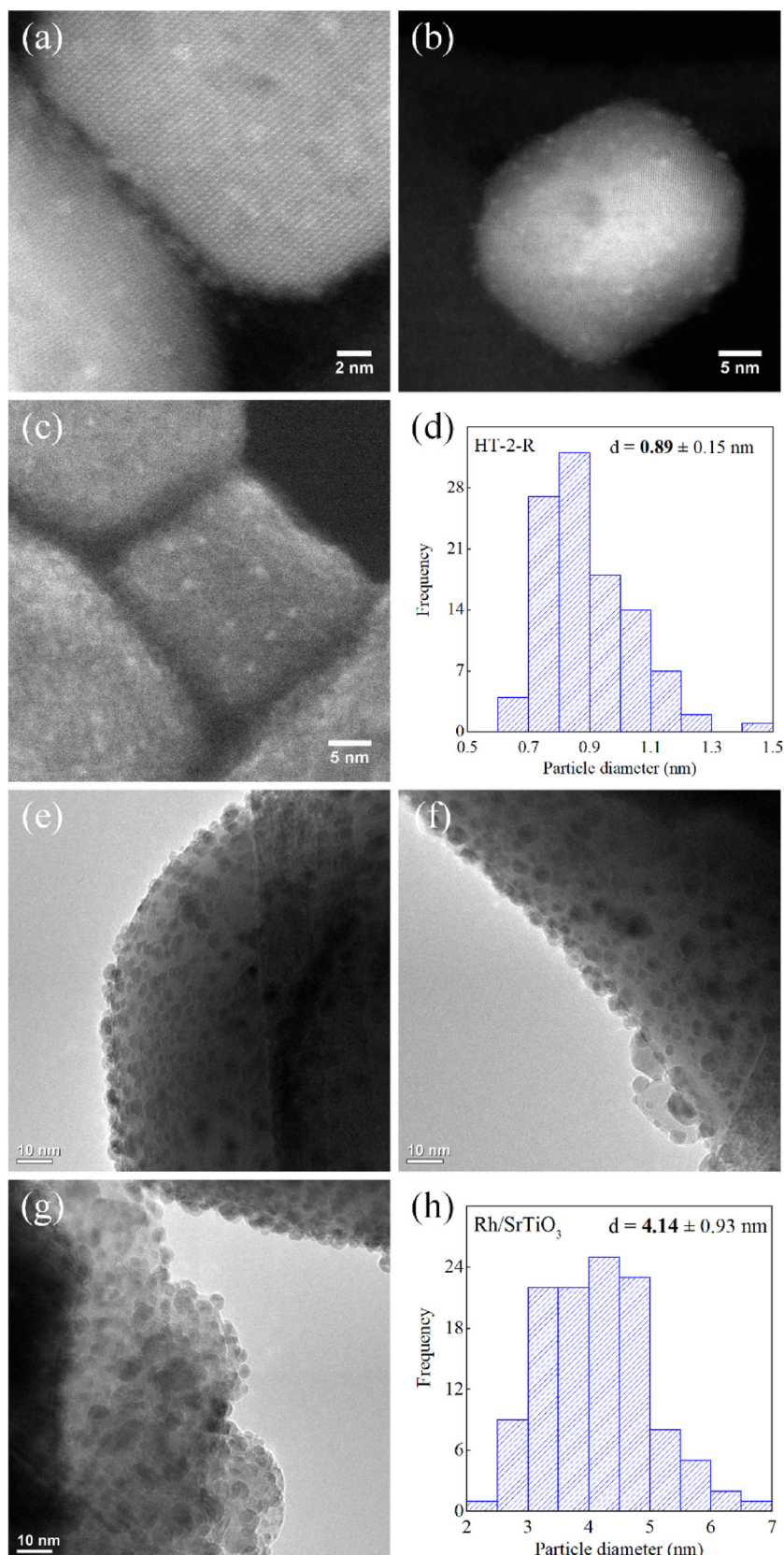


Fig. 4. Representative annular dark-field (ADF-) STEM images (a)-(b), and high-resolution SEM images (c), and the size distribution of Rh nanoparticles (d) of the HT-2-R sample. Representative TEM images (e)-(g) and Rh particle size distribution (h) of the reduced Rh/SrTiO₃ sample.

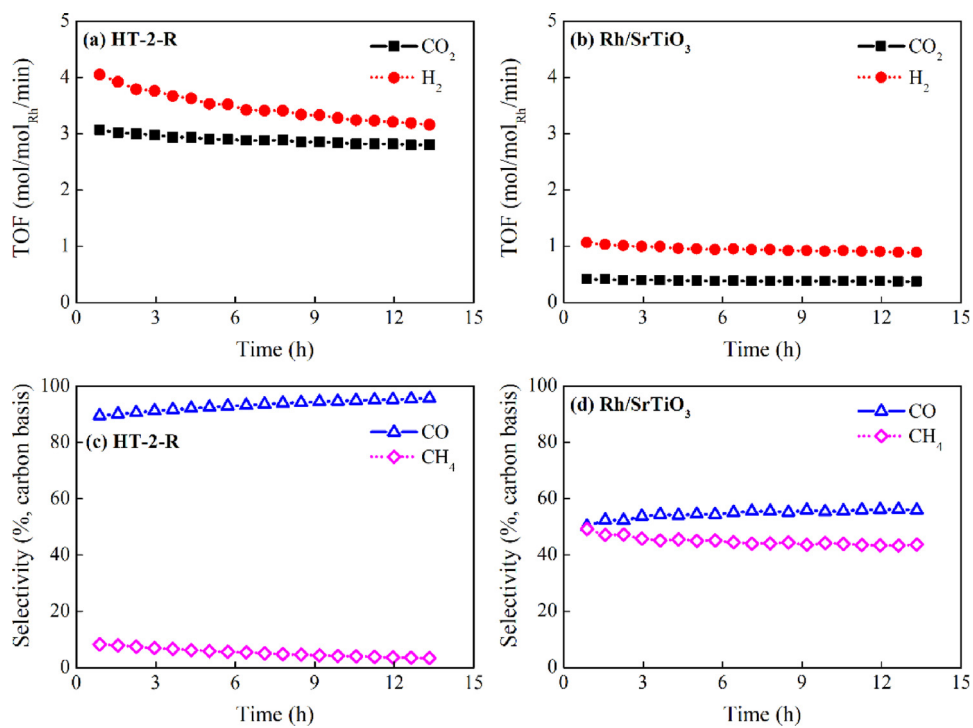


Fig. 5. TOFs of CO₂ and H₂ over (a) HT-2-R and (b) Rh/SrTiO₃, selectivities of CO and CH₄ over (c) HT-2-R and (d) Rh/SrTiO₃ plotted versus time on stream for reaction of CO₂ and H₂ (1:1 ratio, 2 mL/min CO₂ + 2 mL/min H₂ + 36 mL/min Ar, 20 mg HT-2-R, 100 mg Rh/SrTiO₃) at 573 K.

Table 2

Summary of flow reactor results for CO₂ + H₂ reaction (1:1 ratio, 2 mL/min CO₂ + 2 mL/min H₂ + 36 mL/min Ar) at 573 K. Values of conversion, yield, selectivity, TOF and STY calculated by averaging data points between 11–13 h on stream.

Catalyst	HT-2-R (20 mg)	Rh/SrTiO ₃ (20 mg)	Rh/SrTiO ₃ (100 mg)
Conversion, %	CO ₂ H ₂	2.2 11.8	5.0
Yield, % (carbon basis)	CO CH ₄	1.7 0.5	2.8 2.2
Selectivity, % (carbon basis)	CO CH ₄	95.4 21.6	78.1 43.5
TOF ₁ , time/site/min	CO ₂ H ₂	5.7 6.5	4.0 4.6
TOF ₂ , mol/mol _{Rh} /min	CO ₂ H ₂	2.8 3.2	0.8 1.3
STY, mol/mol _{Rh} /min	CO CH ₄	2.70 0.10	0.61 0.17
			0.23 0.17

shown in Fig. 6 and 7, three main broad adsorption bands, located at 1675–1725, 1560–1620, and 1330–1380 cm^{−1}, were clearly observed on HT-2-R during CO₂ hydrogenation. The strong bands at 1560–1620 and 1330–1380 cm^{−1}, corresponding to the antisymmetric and symmetric OCO stretching vibrations, were mainly originated from the carboxylate [30–32] or formate species [30,33–35] (denoted as $^{*}\text{CO}_2^{\delta^-}$). The weak signals at about 1702, 1635, 1410, 1270, 1050 cm^{−1} can be assigned to surface bicarbonate species [29,30,34,36]. In contrast, two strong broad adsorption bands located at 1650–1720 and 1360–1400 cm^{−1} with two weak shoulders at 1560 and 1420 cm^{−1} were observed on Rh/SrTiO₃ during CO₂ hydrogenation. These IR bands had contributions from different vibrational modes of the adsorbed bicarbonate, bidentate and monodentate carbonates [36,37] (denoted as $^{*}\text{CO}_3^{\delta^-}$). According to the relative peak intensity shown in Fig. 6, the $^{*}\text{CO}_3^{\delta^-}$ species, formed due to the interaction of CO₂ with surface oxygen atoms, were the dominant species on Rh/SrTiO₃. However, the $^{*}\text{CO}_2^{\delta^-}$ species were dominant on HT-2-R as CO₂ was

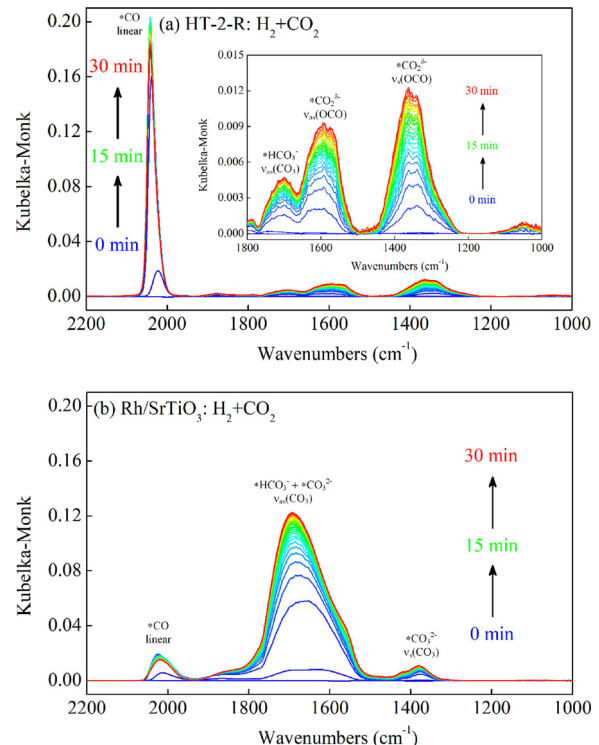


Fig. 6. In-situ DRIFT spectra of CO₂ hydrogenation after H₂ reduction over (a) HT-2-R and (b) Rh/SrTiO₃ in the region of 2100–1000 cm^{−1} (1 mL/min CO₂ + 1 mL/min H₂ + 18 mL/min He, ~15 mg sample, 0.1 MPa, 573 K).

more easily activated on the oxygen vacancy site to form the $^{*}\text{CO}_2^{\delta^-}$ species. After switching the gases from the H₂ + CO₂ mixture to a 5% H₂ flow, the intensities of the $^{*}\text{CO}_2^{\delta^-}$ species on HT-2-R significantly decreased while those of the $^{*}\text{CO}_3^{\delta^-}$ species on Rh/SrTiO₃ were only slightly changed, as shown in Fig. 7. This suggests that the $^{*}\text{CO}_2^{\delta^-}$

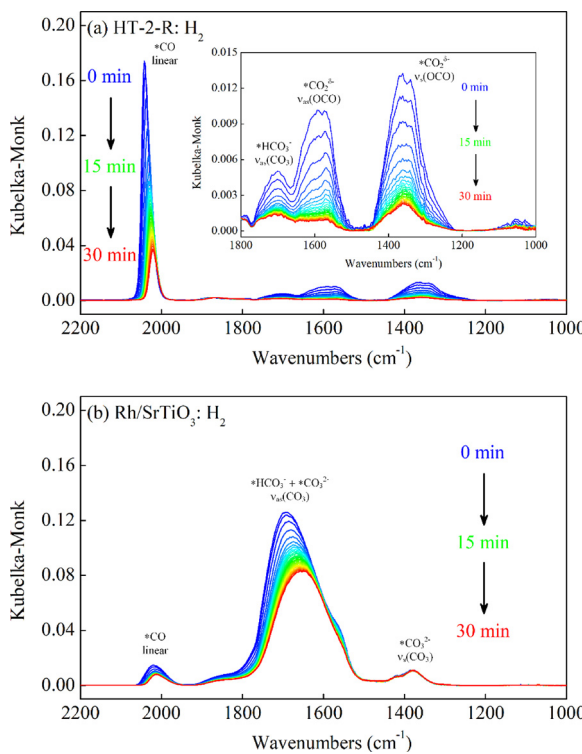


Fig. 7. *In-situ* DRIFT spectra of H_2 treatment after CO_2 hydrogenation over (a) HT-2-R and (b) Rh/SrTiO_3 in the region of $2100\text{--}1000\text{ cm}^{-1}$ (1 mL/min H_2 + 19 mL/min He, ~ 15 mg sample, 0.1 MPa, 573 K).

species on HT-2-R could be the active intermediates for CO_2 activation and conversion as they can be further hydrogenated to the products. However, the $^{*}\text{CO}_3^{2-}$ species on Rh/SrTiO_3 seem to be the inert species since they do not undergo further transformation to desirable products.

The transient evolution of CO adsorption behavior on HT-2-R and Rh/SrTiO_3 at 573 K after gas switching from reactants to a 5% H_2 flow is shown more clearly in Fig. S7. Under reaction conditions, as shown in Fig. 6, the adsorption of CO on HT-2-R (Rh/SrTiO_3) produces two main bands at 2042 (2020) and 1878 (1860) cm^{-1} , which are assigned to linear-adsorbed CO species on Rh [10,11,31,33–35] and bridge-bonded CO species [33–35], respectively. Although the linear Rh–CO peak is dominant in both samples, its intensity on HT-2-R is much stronger than that on Rh/SrTiO_3 . The appearance of strong linear-adsorbed CO peak can be explained by a positive role of highly dispersed subnanometer Rh clusters on HT-2-R as described below. After gas switching, there is a decrease in the intensity of linear Rh–CO peak on HT-2-R (Rh/SrTiO_3) with a concomitant shift to a lower wavenumber, from 2042 (2020) to 2021 (2012) cm^{-1} , whereas the peaks attributed to bridged-bonded CO species do not change appreciably during the transient experiment.

When CO is adsorbed on a metal surface, the electrons are partially transferred from d orbitals of the metal to the antibonding π orbitals of CO (i.e., backdonation). This electron-transfer would strengthen the metal–C bond and weaken the C–O bond [38], likely leading to a decrease in the vibrational frequency of the ν_{CO} band(s). As compared in Fig. S8, the frequency of linear Rh–CO on HT-2-R is higher than that on Rh/SrTiO_3 , either under reaction or H_2 treatment conditions. Higher frequency means less backdonation, likely indicating that the CO binding strength on HT-2-R is weaker than that on Rh/SrTiO_3 . However, it should be noted that the change in the CO stretching frequency could be caused by a convolution of support charge transfer to Rh, Rh existing in the support lattice and structural changes in Rh. Further studies are required to clearly distinguish these contributions. As demonstrated in previous work, the binding energy of CO, a key intermediate in CO_2 hydrogenation reaction, is critical in determining/

controlling the product selectivity and could be a key variable to predict the extent of the CH_4 production via the RWGS + CO-Hydro pathway [5,32]. On HT-2-R, $^{*}\text{CO}$ produced via the RWGS reaction is likely to desorb by overcoming a lower barrier since the CO binding strength is weaker, resulting in a smaller amount of $^{*}\text{CO}$ being available for further hydrogenation to CH_4 . On Rh/SrTiO_3 , the CO binding energy is stronger leading to stronger adsorption, thereby allowing a more facile hydrogenation to CH_4 . Overall, the increased stability of $^{*}\text{CO}$ promotes the reactions via the CO-Hydro pathway to produce CH_4 . Therefore, CO would be the major product for CO_2 hydrogenation on HT-2-R while further hydrogenation of $^{*}\text{CO}$ to CH_4 would be more favorable on Rh/SrTiO_3 . This conclusion agrees well with the steady state flow reactor data that the CO selectivity is much higher (over 95%) for CO_2 hydrogenation on HT-2-R.

The variation of CO binding energy on HT-2-R mainly comes from unique properties of the catalysts produced by the doping-segregation method. Given that the Rh atoms were firstly doped into the SrTiO_3 lattice and then segregated to form surface subnanometer Rh clusters, this synthetic approach unavoidably results in a high concentration of surface defects and strong metal-support interactions (SMSI) [21,22,29]. This SMSI effect not only would enhance the thermal stability of the subnanometer Rh clusters but also lead to unique electronic properties of Rh subnanoclusters, different from those of nanoparticles [11,16]. The formed Rh clusters are usually located on the defects of the support with a Rh–oxygen-cation (support) bonding configuration [39–41], leading to charge transfer between Rh atoms and the SrTiO_3 support due to different chemical potentials [16]. As a result, the anchored Rh atoms would carry some positive charge, which was also verified by various spectral measurements and DFT calculations described in literature [42–44]. As the size of Rh particles is decreased from nanometer to subnanometer scale, the percentage of anchored Rh atoms (Rh^{8+} , less electron rich in d orbitals, less backdonation) would increase dramatically. As a consequence of decreased backdonation from Rh atoms, the terminal Rh–CO band on HT-2-R should shift to higher frequencies, as exhibited in Fig. S8.

The reaction rate of CO_2 and H_2 over the HT-2-R and Rh/SrTiO_3 catalysts at different temperatures with 10 K temperature increment are plotted as a function of $1/T$ in Fig. S9. As evident from the data, HT-2-R is more active for both CO_2 and H_2 conversions over a wide range of temperatures. Due to the fact that CO_2 could be efficiently activated via the $^{*}\text{CO}_2^{2-}$ species on the surface defects (oxygen vacancies) of the HT-2-R catalyst, the apparent activation energy of CO_2 over HT-2-R is smaller than the corresponding value over Rh/SrTiO_3 . Meanwhile, since smaller Rh particle shows better activity for hydrogen dissociation and should accelerate the hydrogenation reaction subsequently [16], the subnanometer Rh clusters on HT-2-R are expected to activate H_2 with a lower activation barrier, as shown in the Arrhenius plot (Fig. S9).

3.3. Catalytic activity of HT-2-R for $\text{CO}_2 + \text{C}_2\text{H}_6$ reaction

Flow reactor experiments of $\text{CO}_2 + \text{C}_2\text{H}_6$ reaction over HT-2-R and Rh/SrTiO_3 were carried out under atmospheric pressure at 823 K. The conversions of CO_2 and C_2H_6 , and yields of CO and C_2H_4 as a function of time on stream for both samples are shown in Fig. S10. The TOF of CO_2 and C_2H_6 , STY of CO and H_2 as a function of time on stream for both samples are shown in Fig. 8. The steady-state conversion, yield, selectivity, turnover frequency (TOF) and space-time yield (STY) are listed in Table 3. As shown in Table 3, both catalysts exhibit a typical reforming activity with over 99% CO selectivity. Compared to the Rh/SrTiO_3 catalyst, the HT-2-R sample presents a much higher activity for the DRE reaction in terms of the steady-state conversion, yield, STY and TOF calculated by normalizing conversion with the Rh loading amount. The TOF that based on the CO uptake value shows an opposite trend, suggesting that the CO adsorption site at room temperature might not be the exact active site for HT-2-R under reaction conditions. As revealed by the *in-situ* XAFS measurements, only 45% of Rh atoms in the

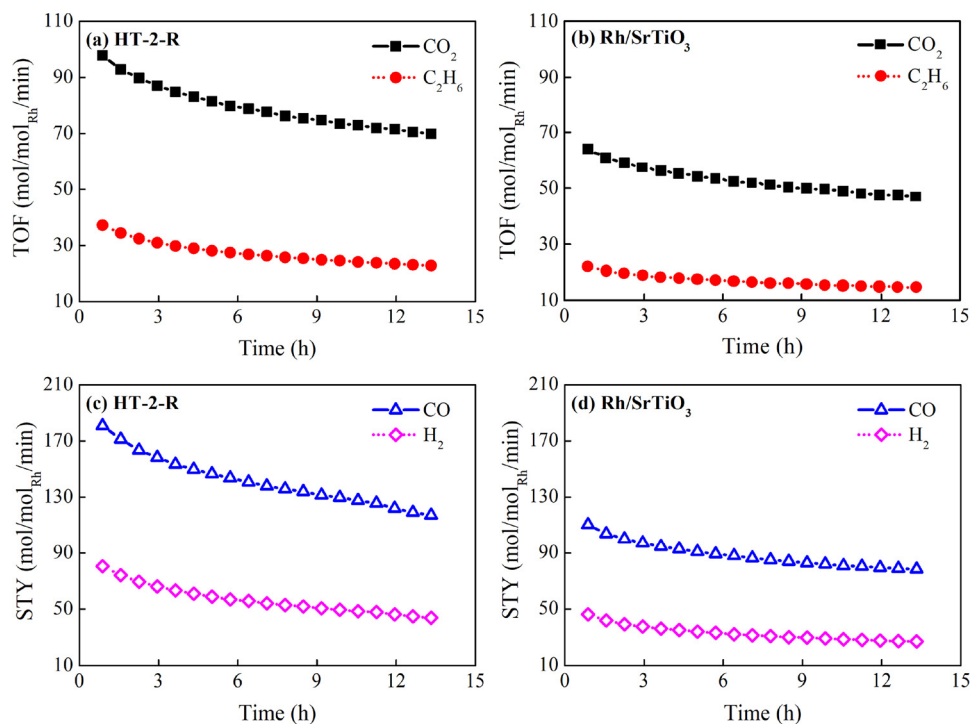


Fig. 8. TOFs of CO₂ and C₂H₆ over (a) HT-2-R and (b) Rh/SrTiO₃, STYs of CO and H₂ over (c) HT-2-R and (d) Rh/SrTiO₃ plotted versus time on stream for reaction of CO₂ and ethane (2:1 ratio, 20 mL/min CO₂ + 10 mL/min C₂H₆ + 10 mL/min Ar, 20 mg catalyst) at 823 K.

Table 3

Summary of flow reactor results for CO₂ + C₂H₆ reaction (2:1 ratio, 20 mL/min CO₂ + 10 mL/min C₂H₆ + 10 mL/min Ar) at 823 K. Values of conversion, selectivity, TOF and STY calculated by averaging data points between 11–13 h on stream.

Catalyst	HT-2-R	Rh/SrTiO ₃
Conversion, %	CO ₂	19.2
	C ₂ H ₆	12.6
Yield, % (ethane basis)	CO	12.48
	CH ₄	0.08
	C ₂ H ₄	0.04
Selectivity, % (ethane basis)	CO	99.1
	CH ₄	0.6
	C ₂ H ₄	0.3
TOF ₁ , time/site/min	CO ₂	144.1
	C ₂ H ₆	47.4
TOF ₂ , mol/mol _{Rh} /min	CO ₂	71.0
	C ₂ H ₆	23.3
STY, mol/mol _{Rh} /min	H ₂	45.7
	CO	121.0
	CH ₄	0.3
	C ₂ H ₄	0.1

lattice of Rh-doped SrTiO₃ can be reduced to metallic Rh. Therefore, the actual TOFs for CO₂ and C₂H₆ on the HT-2-R sample should be as high as 157.8 and 57.8 mol/mol_{surface Rh}/min, respectively, indicating that the formed surface Rh clusters from the lattice of Rh-doped SrTiO₃ are highly active for DRE reaction.

One of the major factors leading to the better performance of HT-2-R for DRE is the small Rh clusters (0.89 ± 0.14 nm) that derived from Rh-doped SrTiO₃ lattice. The Rh particle size trend agrees well with the activity trend: the smaller particle size, the more active site, and the higher DRE activity. Another major factor leading to the excellent performance of HT-2-R for the DRE reaction is the contribution of oxygen vacancies. The formation of oxygen vacancies could be originated from the substitutional doping of Rh atoms to replace Ti atoms in the SrTiO₃ lattice, which was confirmed by the theoretical EXAFS fitting result that the Rh-O coordination number (CN) before reduction

was less than 6. Another possibility is that the formation of oxygen vacancies was accompanied with the reduction/separation of Rh dopant atoms from the lattice of Rh-doped SrTiO₃. The existence of oxygen vacancies on the HT-2-R sample was demonstrated by the CO₂ pulse experiment performed at 823 K, as shown in Fig. 9. The surface oxygen vacancies showed a strong tendency to react with CO₂ under reaction conditions, leading to a direct C–O bond scission to form gas phase CO and surface oxygen species. As shown in Fig. 9, the CO formation on each CO₂ pulse over the HT-2-R sample, which is originated from the reaction of oxygen vacancies with CO₂, was continually recorded. The accumulated CO formation amount represents the consumption amount of the surface oxygen vacancies, which was calculated to be 6.5 μmol/g on the HT-2-R sample. As a comparison, the CO formation was barely seen for the Rh/SrTiO₃ sample synthesized by the traditional wetness impregnation method. The total amount of oxygen vacancies on the reduced Rh/SrTiO₃ catalyst is only 0.05 μmol/g.

The reaction rates of CO₂ and C₂H₆ over the HT-2-R and Rh/SrTiO₃ catalysts at different temperatures with 10 K temperature increment were plotted as a function of 1/T in Fig. S11. It is apparent that the HT-2-R catalyst is more active than Rh/SrTiO₃ catalyst for DRE reaction

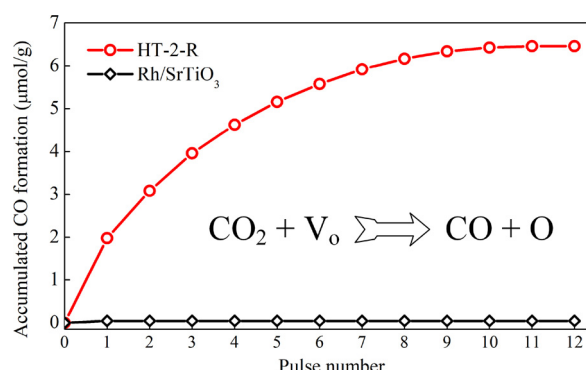


Fig. 9. Accumulated CO formation amount for the HT-2-R and Rh/SrTiO₃ catalysts during CO₂ pulse experiments.

over a wide range of temperatures. As shown in the Arrhenius plot, the apparent activation energies of C_2H_6 for both samples are very close, indicating that the ethane activation mechanism is likely the same for both catalysts. This also suggests that the dry reforming of ethane over Rh particles is a structure-insensitive reaction since the particle size of Rh clusters varies greatly on these two samples. However, smaller Rh particles would provide more active sites, leading to higher activities. The activation energy of CO_2 over HT-2-R is smaller than the corresponding value over Rh/SrTiO₃. This is due to the fact that the existence of oxygen vacancies on the HT-2-R sample that is highly active for CO_2 conversion with a lower activation barrier. Therefore, the highly dispersed Rh clusters and the formation of surface oxygen vacancies as a consequence of the segregation of Rh dopant atoms were revealed to be responsible for the better performance of catalyst prepared by the doping-segregation method for the DRE reaction.

4. Conclusions

The subnanometer Rh clusters derived from Rh-doped SrTiO₃ have been successfully synthesized by a doping-segregation method and demonstrated to be highly active catalysts for CO_2 reduction by hydrogenation and ethane. Compared to the Rh/SrTiO₃, the HT-2-R catalyst exhibits a larger space-time yield as well as selectivity to CO for the $CO_2 + H_2$ reaction at 573 K, and a higher activity for the $CO_2 + C_2H_6$ reaction at 823 K. The superior catalytic activity is revealed to be attributed to the synergistic effects of highly dispersed subnanometer Rh clusters providing more sites for H_2/C_2H_6 dissociation/activation and surface oxygen vacancies efficiently promoting the adsorption/activation of CO_2 . The enhanced CO selectivity for CO_2 hydrogenation can be explained by a weaker binding of CO on Rh caused by the strong interactions (e.g., charge transfer) between Rh atoms and the oxide support containing surface defects. Adjusting such parameters as size of active metal clusters, the physicochemical properties of support, and the interactions between the active metal atoms and the oxide support; can be potentially used to tune the adsorption, activation, and reaction behavior of reactants. The new knowledge developed in this work may offer a strategy to design novel catalysts with high activity and desired selectivity for a variety of chemical reactions.

Acknowledgments

The work is sponsored by the U.S. Department of Energy (DOE), Office of Science, Office of Basic Energy Sciences, Division of Chemical Sciences, Biosciences and Geosciences, under Contract No. DE-SC0012704 and the National Natural Science Foundation of China (NSFC) under Grant No. 21673125. This research project has been supported by the NSF DMR Award 1254600. Use of the Stanford Synchrotron Radiation Lightsource, SLAC National Accelerator Laboratory, is supported by the U.S. Department of Energy, Office of Science, Office of Basic Energy Sciences under Contract No. DE-AC02-76SF00515. This research used resources of the Center for Functional Nanomaterials, which is a U.S. DOE Office of Science Facility, at Brookhaven National Laboratory under Contract No. DE-SC0012704. A.I.F. acknowledges support of the U.S. Department of Energy Grant No. DE-FG02-03ER15476 and Program Development funding at Brookhaven National Laboratory. Operations at the Beamline BL2-2 in SSRL were supported in part by the Synchrotron Catalysis Consortium (U.S. Department of Energy, Office of Basic Energy Sciences, Grant No. DESC0012335).

Appendix A. Supplementary data

Supplementary material related to this article can be found, in the online version, at doi:<https://doi.org/10.1016/j.apcatb.2018.06.074>.

References

- [1] M.D. Porosoff, B.H. Yan, J.G.G. Chen, *Energy Environ. Sci.* 9 (2016) 62–73.
- [2] W. Wang, S. Wang, X. Ma, J. Gong, *Chem. Soc. Rev.* 40 (2011) 3703–3727.
- [3] E.V. Kondratenko, G. Mul, J. Baltrusaitis, G.O. Larrazabal, J. Perez-Ramirez, *Energy Environ. Sci.* 6 (2013) 3112–3135.
- [4] M.D. Porosoff, X. Yang, J.A. Boscoboinik, J.G. Chen, *Angew. Chem.* 53 (2014) 6705–6709.
- [5] S. Kattel, W. Yu, X. Yang, B.H. Yan, Y. Huang, W. Wan, P. Liu, J.G. Chen, *Angew. Chem.* 55 (2016) 7968–7973.
- [6] M. Myint, B.H. Yan, J. Wan, S. Zhao, J.G. Chen, *J. Catal.* 343 (2016) 168–177.
- [7] B.H. Yan, X.F. Yang, S.Y. Yao, J. Wan, M. Myint, E. Gomez, Z.H. Xie, S. Kattel, W.Q. Xu, J.G.G. Chen, *ACS Catal.* 6 (2016) 7283–7292.
- [8] M.D. Porosoff, J.G.G. Chen, *J. Catal.* 301 (2013) 30–37.
- [9] J.C. Matsubu, V.N. Yang, P. Christopher, *J. Am. Chem. Soc.* 137 (2015) 3076–3084.
- [10] D. Heyl, U. Rodemerck, U. Bentrup, *ACS Catal.* 6 (2016) 6275–6284.
- [11] J.C. Matsubu, S. Zhang, L. DeRita, N.S. Marinkovic, J.G. Chen, G.W. Graham, X. Pan, P. Christopher, *Nat. Chem.* 9 (2017) 120–127.
- [12] F. Solymosi, P. Tolmacsov, K. Kedves, *J. Catal.* 216 (2003) 377–385.
- [13] M. Nagai, K. Nakahira, Y. Ozawa, Y. Namiki, Y. Suzuki, *Chem. Eng. Sci.* 62 (2007) 4998–5000.
- [14] D. Pakhare, J. Spivey, *Chem. Soc. Rev.* 43 (2014) 7813–7837.
- [15] S. Kattel, B.H. Yan, J.G. Chen, P. Liu, *J. Catal.* 343 (2016) 115–126.
- [16] X.F. Yang, A. Wang, B. Qiao, J. Li, J. Liu, T. Zhang, *Acc. Chem. Res.* 46 (2013) 1740–1748.
- [17] Y. Lei, F. Mahmood, S. Lee, J. Greeley, B. Lee, S. Seifert, R.E. Winans, J.W. Elam, R.J. Meyer, P.C. Redfern, D. Teschner, R. Schlogl, M.J. Pellin, L.A. Curtiss, S. Vajda, *Science* 328 (2010) 224–228.
- [18] A.A. Herzing, C.J. Kiely, A.F. Carley, P. Landon, G.J. Hutchings, *Science* 321 (2008) 1331–1335.
- [19] W.E. Kaden, T. Wu, W.A. Kunkel, S.L. Anderson, *Science* 326 (2009) 826–829.
- [20] B. Qiao, L. Liu, J. Zhang, Y.Q. Deng, *J. Catal.* 261 (2009) 241–244.
- [21] Y. Nishihata, J. Mizuki, T. Akao, H. Tanaka, M. Uenishi, M. Kimura, T. Okamoto, N. Hamada, *Nature* 418 (2002) 164–167.
- [22] H. Tanaka, M. Taniguchi, M. Uenishi, N. Kajita, I. Tan, Y. Nishihata, J. Mizuki, K. Narita, M. Kimura, K. Kaneko, *Angew. Chem.* 45 (2006) 5998–6002.
- [23] D. Neagu, G. Tsekouras, D.N. Miller, H. Menard, J.T.S. Irvine, *Nat. Chem.* 5 (2013) 916–923.
- [24] Q. Wu, B. Yan, J. Cen, J. Timoshenko, D.N. Zakharov, X. Chen, H.L. Xin, S. Yao, J.B. Parise, A.I. Frenkel, E.A. Stach, J.G. Chen, A. Orlov, *Chem. Mater.* (2018).
- [25] W.R. Woerner, A.M. Plonka, X.Y. Chen, D. Banerjee, P.K. Thallapally, J.B. Parise, *J. Phys. Chem. C* 120 (2016) 360–369.
- [26] A.I. Frenkel, C.W. Hills, R.G. Nuzzo, *J. Phys. Chem. B* 105 (2001) 12689–12703.
- [27] B. Ravel, M. Newville, *J. Synchrotron. Radiat.* 12 (2005) 537–541.
- [28] R. Niishiro, S. Tanaka, A. Kudo, *Appl. Catal. B-Environ.* 150 (2014) 187–196.
- [29] Q. Wu, J. Cen, K.R. Goodman, M.G. White, G. Ramakrishnan, A. Orlov, *ChemSusChem* 9 (2016) 1889–1897.
- [30] S. Chen, T. Cao, Y. Gao, D. Li, F. Xiong, W. Huang, *J. Phys. Chem. C* 120 (2016) 21472–21485.
- [31] J. Rasko, F. Solymosi, *J. Phys. Chem.* 98 (1984) 7147–7152.
- [32] S. Kattel, B. Yan, Y. Yang, J.G. Chen, P. Liu, *J. Am. Chem. Soc.* 138 (2016) 12440–12450.
- [33] H. Kusama, K. Okabe, H. Arakawa, *Appl. Catal. Gen.* 207 (2001) 85–94.
- [34] J. Scalbert, F.C. Meunier, C. Daniel, Y. Schuurman, *Phys. Chem. Chem. Phys. : PCCP* 14 (2012) 2159–2163.
- [35] A. Karelovic, P. Ruiz, *J. Catal.* 301 (2013) 141–153.
- [36] L. Mino, G. Spoto, A.M. Ferrari, *J. Phys. Chem. C* 118 (2014) 25016–25026.
- [37] D. Cornu, H. Guesmi, J.-M. Krafft, H. Lauron-Pernot, *J. Phys. Chem. C* 116 (2012) 6645–6654.
- [38] A. Erdöhelyi, F. Solymosi, *J. Catal.* 84 (1983) 446–460.
- [39] S. Wang, A.Y. Borisevich, S.N. Rashkeev, M.V. Glazoff, K. Sohlberg, S.J. Pennycook, S.T. Pantelides, *Nat. Mater.* 3 (2004) 143–146.
- [40] S.F. Hackett, R.M. Brydson, M.H. Gass, I. Harvey, A.D. Newman, K. Wilson, A.F. Lee, *Angew. Chem.* 46 (2007) 8593–8596.
- [41] B. Qiao, A. Wang, X. Yang, L.F. Allard, Z. Jiang, Y. Cui, J. Liu, J. Li, T. Zhang, *Nat. Chem.* 3 (2011) 634–641.
- [42] Q. Fu, H. Saltsburg, M. Flytzani-Stephanopoulos, *Science* 301 (2003) 935–938.
- [43] V. Shapovalov, H. Metiu, *J. Catal.* 245 (2007) 205–214.
- [44] Z.P. Hu, H. Metiu, *J. Phys. Chem. C* 115 (2011) 17898–17909.